

# Development of flexible designs for PVFC hybrid power systems



Vincentius Surya Kurnia Adi, Chuei–Tin Chang\*

Department of Chemical Engineering, National Cheng Kung University, Tainan 70101, Taiwan, ROC

## ARTICLE INFO

### Article history:

Received 14 April 2014

Accepted 1 August 2014

Available online 23 August 2014

### Keywords:

Flexibility index

Resilient design

Hybrid power generation system

## ABSTRACT

Extensive studies have already been performed in the past to integrate more than one 'green' energy source, e.g., solar, wind and hydrogen, for power generation. For actual operation in a realistic environment, such a hybrid process must be fully functional despite random fluctuations in energy supplies and power demands. A common option for accommodating the uncertain disturbances and their cumulative effects is to introduce battery into a properly structured system. However, by using an ad hoc approach, these schemes may be either overdesigned or inoperable. A generic mathematical programming model is thus adopted in the present study to compute a so-called *temporal flexibility index* for use as a performance measure. In order to demonstrate the usefulness of this assessment criterion, a large collection of photovoltaic–fuel cell (PVFC) systems can be configured for a specific application and then compared accordingly so as to identify the best combination of energy supply ratio and battery capacity. A MATLAB/Simulink simulation program has also been developed in this work to validate these design decisions.

© 2014 Elsevier Ltd. All rights reserved.

## 1. Introduction

As the alternatives to fossil fuels, various renewable energy sources, such as solar, wind and hydrogen, etc., have attracted increasing attention in recent years. Among the currently viable options, the photovoltaic (PV) generator that directly converts solar energy into electricity has often been utilized in low-power applications. The incentives of this choice are multifaceted, such as being inexhaustible and carbon free, silent, without moving parts, and with size-independent electric conversion efficiency, etc. However, it is also widely recognized that the PV generator alone is not suitable for off-grid applications due to the uncertain nature of solar irradiation. One way to overcome this practical problem is to configure a hybrid power system driven by the solar energy and also at least one other more stable source [1]. The fuel cell (FC) is clearly a good candidate since it is blessed with high efficiency and quick response [2] and its applicability has already been successfully demonstrated. Although numerous studies on the optimization, modeling and design of the photovoltaic–fuel cell (PVFC) systems have already been carried out, e.g., see El-Aal [3], Li et al. [4] and Tesfahunegn [5], none of them considered the important issue of operational flexibility. According to the literature review

conducted by Banos et al. [6], the published optimization studies on the renewable/sustainable energy systems have never incorporated any form of flexibility indicator as the objective function. Finally, Bajpai and Dash [7] also reviewed numerous works on the hybrid systems for power generation in stand-alone applications, but identified no procedures for quantifying system flexibility.

Although incorporation of a large enough battery usually facilitates resilient operation [1], it is important to optimally allocate the capacities of individual components in the PVFC system so as to avoid overdesign. For this purpose, a quantitative flexibility measure is adopted in the present study to reflect the ability of a given system to maintain feasible operation despite uncertain variations in the process parameters [8]. Swaney and Grossmann [9,10] proposed a mixed-integer nonlinear program to calculate the *steady-state flexibility index* ( $FI_s$ ) for the continuous processes. As suggested later by Dimitriadis and Pistikopoulos [8], the operational flexibility of a dynamic system should be determined in a similar fashion. By adopting a set of differential algebraic equations (DAEs) as the equality constraints, they developed a modified formulation for computing the *dynamic flexibility index* ( $FI_d$ ). Clearly this practice is more rigorous than that based on the steady-state model since, even for a continuous process, the operational flexibility cannot be adequately characterized without accounting for the transient dynamics.

In the above dynamic flexibility analysis, the nominal values of uncertain parameters and the anticipated positive and negative deviations in these parameters were assumed to be available at

\* Corresponding author.

E-mail addresses: [ctchang@mail.ncku.edu.tw](mailto:ctchang@mail.ncku.edu.tw), [chueitinchang@msn.com](mailto:chueitinchang@msn.com) (C. Chang).

every instance over the entire operation horizon. The corresponding flexibility index can be uniquely determined on the basis of a dynamic system model and also such a priori information. However, while the unexpected fluctuations in process parameters may render an ill-designed system inoperable at certain point in time, their cumulative effects can also result in serious consequences. The latter scenario has been ignored in computing  $FI_d$ . In a recent study, Adi and Chang [11,12] developed a generic mathematical program to compute a *temporal flexibility index* ( $FI_t$ ) for quantifying the system's ability to buffer both instantaneous and accumulated changes in process parameters. This upgraded performance measure is utilized as a design criterion for identifying realistic PVFC system configurations in the present study.

The rest of the paper is organized as follows. The mathematical models of PVFC system are first presented in the next section. In Section 3, the novel concept of temporal flexibility is outlined and a generic programming formulation (for computing  $FI_t$ ) is also given. A series of case studies have been performed to validate the proposed design approach in this work. The optimization and simulation results on the PVFC system in Fig. 1 are thoroughly analyzed and discussed in Section 4. Finally, conclusions are drawn in Section 5.

## 2. Mathematical model of PVFC system

As shown in Fig. 1, a PVFC system is basically made of three components, i.e., a solar module, a polymer electrolyte membrane (PEM) fuel cell, and a battery. If the solar and fuel cells collectively generate more power than the load requires, the excess current is diverted towards the battery and subsequently stored for later use. The mathematical models of these basic units are presented below:

### • Photovoltaic cells

The photovoltaic module typically consists of several cells connected in series. The conventional modeling approach is to describe the p–n junction physics in the form of *equivalent circuits*. A typical version of this circuit is given in Fig. 2 [13] and the cell current  $I_{PV}$  can be calculated accordingly, i.e.

$$I_{PV} = I_{ph} - I_{d1} - I_{d2} - I_p \quad (1)$$

where,  $I_{ph}$  denotes the light-generated current (which is a function of solar radiation and cell temperature);  $I_{d1}$  denotes the diffusion current from the base to emitter layers;  $I_{d2}$  represents the effect of the generation and re-combination current in the junction space charge region;  $I_p$  represents the current flowing through the shunt resistance ( $R_p$ ), which can be viewed as the effect of leakage current flowing across the junction between the n and p layers. Notice also that, in this equivalent circuit, the series resistance  $R_s$  is used to

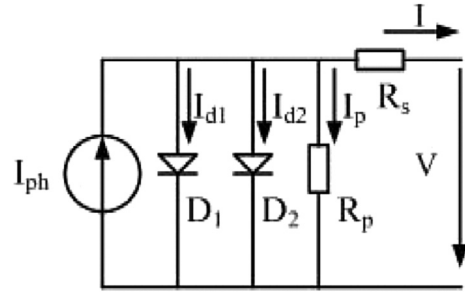


Fig. 2. Equivalent circuit of a solar cell [13].

represent the losses due to current flowing through the highly resistive emitter and contacts, and  $V$  and  $I$  denote the terminal voltage and current of the solar cell, respectively.

Explicit formulas for computing the right-side terms of equation (1) are outlined below. Specifically,

1.  $I_{ph}$ :

$$I_{ph} = I_{phref} \frac{S}{S_{ref}} \left[ 1 - \alpha (T_c - T_{cref}) \right] \quad (2)$$

where,  $I_{phref}$  ( $=8.21$  A) denotes the photocurrent at the standard testing condition (i.e., the irradiation rate of  $1000$  W/m<sup>2</sup> at the solar spectrum of AM 1.5 and the cell temperature of  $25$  °C);  $S$  denotes the solar irradiation rate and  $S_{ref}$  is its reference value ( $=1000$  W/m<sup>2</sup>);  $\alpha$  is the current temperature coefficient ( $=0.0032$  A/°C);  $T_c$  and  $T_{cref}$  represent the cell temperature and its reference level ( $=25$  °C), respectively.

2.  $I_{d1}$ :

$$I_{d1} = k_s T_c^3 \exp\left(-\frac{E_g}{n_1 k T_c}\right) \left[ \exp\left(\frac{V + IR_s}{n_1 V_t}\right) - 1 \right] \quad (3)$$

where,  $k_s$  represents the photocurrent losses due to charge carrier diffusion (which can be obtained by parameter fitting to the  $I$ – $V$  characteristics);  $n_1$  denotes the diode ideality factor (which is usually set to 1);  $E_g$  denotes the material bandgap energy ( $=1.12$  eV for silicon);  $V_t$  denotes the thermal voltage, which is a function of the cell temperature  $T_c$ , the Boltzmann's constant ( $k = 1.38 \times 10^{-23}$ ) and the charge of the electron ( $q = 1.6 \times 10^{-19}$ ), i.e.,  $V_t = kT_c/q$ .

3.  $I_{d2}$ :

$$I_{d2} = k_r T_c^{5/2} \exp\left(-\frac{E_g}{n_2 k T_c}\right) \left[ \exp\left(\frac{V + IR_s}{n_2 V_t}\right) - 1 \right] \quad (4)$$

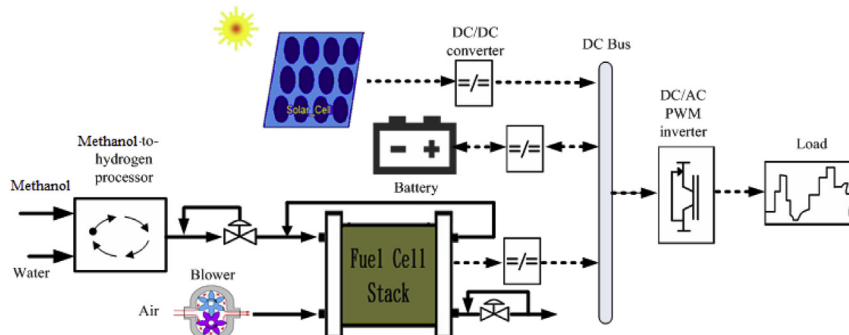


Fig. 1. Hybrid power generation system.

where,  $k_r$  reflects the photocurrent losses due to charge carrier recombination (which can be obtained by parameter fitting to the  $I$ – $V$  characteristics as well);  $n_2$  denotes another diode ideality factor (which is usually set to 2).

4.  $I_p$ :

$$I_p = \frac{V + IR_s}{R_p} \quad (5)$$

The two-diode model can be simplified into the one-diode model in which  $I_{d2}$  is omitted according to Shockley theory [14,15]. Thus the cell current in equation (1) becomes:

$$I_{PV} = I_{ph} - I_{d1} - I_p \quad (6)$$

Since  $R_p$  is usually very large and  $R_s$  is very small,  $I_p$  can be ignored in equation (6) and the resulting simplified one-diode model is

$$I_{PV} = I_{ph} - I_{d1} \quad (7)$$

Equations (1), (6) and (7) are widely accepted as the models for PV system design and performance analysis [13]. In particular, equation (7) is used as the main model for PV module in the current work.

#### • Fuel cells

In an operating fuel cell, the actual voltage  $U_{FC}$  should be lower than its open-circuit voltage  $U_{OCV}$  due to various irreversible mechanisms. Specifically, these losses are originated from (1) the activation overpotential  $\eta_{act}$ , (2) the concentration overpotential  $\eta_{conc}$ , and (3) the Ohmic overpotential  $\eta_{ohm}$ . The actual cell voltage should therefore be expressed as [16]:

$$U_{FC} = U_{OCV} - \eta_{act} - \eta_{conc} - \eta_{ohm} \quad (8)$$

The open-circuit voltage  $U_{OCV}$  can be represented as a change in Gibbs free energy due to the reaction between hydrogen and oxygen. At conditions different from the standard conditions, it is given by:

$$U_{OCV} = 1.2297 + (T_{FC} - 298.15) \frac{\Delta G_0}{2F} + \frac{RT_{FC}}{2F} \ln \left( \frac{p_{H_2} \times p_{O_2}^{1/2}}{p_o^{3/2}} \right) \quad (9)$$

where,  $\Delta G_0$  is the change in Gibbs free energy at standard condition;  $R$  denotes the gas constant whose value is  $8.314 \text{ J K}^{-1} \text{ mol}^{-1}$ ;  $p_{H_2}$  is the partial pressure of hydrogen;  $p_{O_2}$  is the partial pressure of oxygen;  $p_o$  is the operating pressure;  $F$  is the Faraday's constant ( $=9.648 \times 10^4 \text{ C/mol}$ );  $T_{FC}$  is the fuel cell temperature. Based on the ideal gas law and the principle of mole conservation, the partial pressures of hydrogen ( $p_{H_2}$ ) and oxygen ( $p_{O_2}$ ) associated with reactant flow rates at the anode and cathode along with the cell current are modeled as follows [17]:

$$\frac{dp_{H_2}}{dt} = \frac{RT_{FC}}{V_{anode}} \left[ F_{H_2} - k_{anode}(p_{H_2} - p_{H_2,in}) - \frac{15}{F} I_{FC} \right] \quad (10)$$

$$\frac{dp_{O_2}}{dt} = \frac{RT_{FC}}{V_{cathode}} \left[ F_{O_2} - k_{cathode}(p_{O_2} - p_{BPR}) - \frac{7.5}{F} I_{FC} \right] \quad (11)$$

where,  $V_{anode}$  and  $V_{cathode}$  denote the volumes of anode and cathode respectively;  $F_{H_2}$  and  $F_{O_2}$  denote the molar flow rates of hydrogen and oxygen respectively;  $k_{anode}$  ( $=6.5 \times 10^{-2} \text{ mol/s atm}$ ) and  $k_{cathode}$  ( $=6.5 \times 10^{-2} \text{ mol/s atm}$ ) represent the flow constants of anode and cathode, respectively;  $p_{BPR}$  is the cell back pressure ( $=1 \text{ atm}$ ).

The activation overpotential of a fuel cell ( $\eta_{act}$ ) can be attributed to the slowness of the reactions that take place on the surface of the electrodes. The electrode activation of a fuel cell can be described by the Butler–Volmer equation [18]:

$$j = j_o \left[ \exp \left( \frac{2\beta F}{RT_{FC}} \eta_{act} \right) - \exp \left( \frac{2(1-\beta)F}{RT_{FC}} \eta_{act} \right) \right] \quad (12)$$

where,  $\beta$  is the transfer coefficient ( $=0.25$ );  $j$  is the electrical current density;  $j_o$  is the exchange current density on the catalytic surfaces and it is closely related to the operation temperature and the reactant concentration [19,20], i.e.,

$$j_o = j_o^{\text{ref}} (C_{O_2})^\beta (C_{H_2O})^{1-\beta} \exp \left[ -\frac{\Delta G}{R} \left( \frac{298.15 T_{FC}}{298.15 - T_{FC}} \right) \right] \quad (13)$$

where,  $C_{O_2}$  and  $C_{H_2O}$  denote the concentrations of oxygen and water vapor respectively;  $j_o^{\text{ref}}$  is the standard exchange current density;  $\Delta G$  is the change in Gibbs free energy.

On the other hand, the concentration loss is related to the drop of concentration level in the gas channels. The fuel and oxidant are consumed at the surface of the electrodes. The incoming gas must then take the place of the used reactant. The concentrations of fuel and oxidant are reduced at the various points in the gas channels to levels lower than those at the inlet valve of the stack. These losses become significant at higher currents when the consumption rates of fuel and oxidant are higher and the concentrations in the gas channel are at minima.

$$\eta_{\text{conc,anode}} = \frac{RT_{FC}}{2F} \ln \left( 1 - \frac{j_{\text{anode}}}{j_L} \right) \quad (14)$$

$$\eta_{\text{conc,cathode}} = \frac{RT_{FC}}{4F} \ln \left( 1 - \frac{j_{\text{cathode}}}{j_L} \right) \quad (15)$$

where  $\eta_{\text{conc,anode}}$  and  $\eta_{\text{conc,cathode}}$  respectively denote the concentration overpotentials in anode and cathode;  $j_{\text{anode}}$ ,  $j_{\text{cathode}}$  and  $j_L$  are the anode, cathode, and internal current density respectively.

Finally, the Ohmic losses are associated with the resistances due to (i) the flow of electrons (electrical current) through the electrical conductors and (ii) the flow of protons (ionic current) in the electrolyte membrane [21]. The former overpotential follows the Ohm's law:

$$\eta_{\text{ohm,e}} = I_{FC} R_{ec} \quad (16)$$

where,  $I_{FC}$  is the current density flowing through the cell and  $R_{ec}$  is the equivalent electrical resistance. As for the Ohmic loss due to the transport of the protons in the electrolyte membrane, its overpotential ( $\eta_{\text{ohm,m}}$ ) can be expressed as:

$$\eta_{\text{ohm,m}} = I_{FC} R_{ic} \quad (17)$$

where  $R_{ic}$  is the ionic resistance in the electrolyte membrane, which can be calculated as follows:

$$R_{ic} = \frac{d_e}{\sigma_m A_c} \quad (18)$$

where,  $d_e$  denotes the electrode gap width;  $A_c$  denotes the cross-section area of the electrolyte body;  $\sigma_m$  is the ionic conductivity of the electrolyte membrane. The ionic conductivity of the electrolyte membrane is calculated according to the following formula [22,23]:

$$\sigma_m = (0.005139\lambda - 0.00326)\exp\left[1268\left(\frac{1}{303} - \frac{1}{T}\right)\right] \quad (19)$$

where,  $\lambda (=0.043 + 17.8\phi - 39.85\phi^2 + 36.0\phi^3)$  is the water content of the electrolyte membrane;  $\phi$  is the activity of water vapor. Thus, the total Ohmic overpotential in the fuel cell can be represented by:

$$\eta_{ohm} = \eta_{ohm,e} + \eta_{ohm,m} \quad (20)$$

If the hydrogen input and operating temperature of FC module is kept constant, the FC module current can be approximated by  $I_{FC} \approx k_{FC}F_{H_2}$ , and  $k_{FC} (=1.531 \text{ Ah/kmol})$  is an empirical constant for FC module current.

#### • Battery

The discharge model of Li-ion battery is adopted from Tremblay and Dessaint [24], which accurately depicts the voltage dynamics when the current varies. The battery voltage is characterized as:

$$V_{batt} = E_0 - V_{pol}it - R_i I_{batt} + A \exp(-Bit) - R_{pol}I_{batt}^* \quad (21)$$

where,  $V_{batt}$  denotes the battery voltage;  $E_0$  is a reference constant ( $=12 \text{ V}$ );  $V_{pol} = K_V Q/Q - it$  is the polarization voltage;  $R_{pol} = K_R Q/Q - it$  is the polarization resistance;  $K_V (=0.0076 \text{ } \Omega)$  and  $K_R (=0.0076 \text{ } \Omega)$  denote the polarization voltage and resistance constants respectively;  $Q$  is the battery capacity ( $= \text{Ah}$ );  $A$  is the exponential zone amplitude ( $=12.9646 \text{ V}$ );  $B$  is the inverse of zone time constant ( $=0.294783 \text{ A}$ );  $R_i$  is the internal resistance ( $=0.02 \text{ } \Omega$ );  $I_{batt}$  denotes the battery current;  $I_{batt}^*$  denotes the filtered current which determined using the first order low-pass filter;  $it = \int I_{batt} dt$  represents the actual battery charge or

$$\frac{dit}{dt} = I_{batt} \quad (22)$$

On the other hand, note that the voltage increases rapidly when the Li-ion batteries reaches the full charge. This phenomenon is modeled with the polarization resistance term. In the charge mode, the polarization resistance increases until the battery is almost full ( $it \approx 0$ ). Above this point, the polarization resistance should rise abruptly. Instead of the polarization resistance in the discharge model, i.e., equation (19), the polarization resistance should be expressed as:

$$R_{pol} = K_R \frac{Q}{it} \quad (23)$$

Note that, when  $it \rightarrow 0$ , the polarization resistance clearly should approach infinity. However, this is not exactly the case in practice. Experimental results have shown that the contribution of the polarization resistance is shifted by about 10% of the capacity of the battery. In the charging model, instead of the last term on the right side of equation (19), the polarization resistance should actually be replaced by:

$$R_{pol,charge} = K_R \frac{Q}{it - 0.1Q} \quad (24)$$

More specifically, the charging model used in the present study can be expressed as.

$$V_{batt} = E_0 - V_{pol}it - R_i I_{batt} + A \exp(-Bit) - R_{pol,charge} I_{batt}^* \quad (25)$$

The corresponding *state of charge* (SOC) is then formulated as:

$$\text{SOC} = 100 \left(1 - \frac{it}{Q}\right) \quad (26)$$

Finally, three sets of additional constraints must also be imposed, i.e., (1) the minimum no-load battery voltage is 7 V and the maximum battery voltage is  $3E_0$ , (2) the minimum capacity of the battery is 0 Ah and the maximum capacity is  $Q$ , and (3) the maximum discharge current is  $I_{batt}^{\max} = 120I_{batt}^{\text{nom}}$ .

### 3. Temporal flexibility analysis

To facilitate clear explanation of the temporal flexibility concept, let us first review the conventional formulations for flexibility analysis. For illustration convenience, the following label sets should be defined:

$$\mathbb{I} = \{i | i \text{ is the label of an equality constraint}\} \quad (27)$$

$$\mathbb{J} = \{j | j \text{ is the label of an inequality constraint}\} \quad (28)$$

The general design models adopted for the continuous processes can be expressed accordingly as.

$$f_i(\mathbf{d}, \mathbf{z}, \mathbf{x}, \boldsymbol{\theta}) = 0, \quad \forall i \in \mathbb{I} \quad (29)$$

$$g_j(\mathbf{d}, \mathbf{z}, \mathbf{x}, \boldsymbol{\theta}) \leq 0, \quad \forall j \in \mathbb{J} \quad (30)$$

Note that only algebraic constraints are considered here. In addition, with a set of nominal parameter values in vector  $\boldsymbol{\theta}^N$  and the corresponding expected deviations in the positive and negative directions ( $\Delta\boldsymbol{\theta}^+$  and  $\Delta\boldsymbol{\theta}^-$ ), the uncertain parameters can be constrained as.

$$\boldsymbol{\theta}^N - \delta\Delta\boldsymbol{\theta}^- \leq \boldsymbol{\theta} \leq \boldsymbol{\theta}^N + \delta\Delta\boldsymbol{\theta}^+ \quad (31)$$

where,  $\delta$  is a positive scalar variable to be maximized in the *steady-state flexibility index model* [9,10].

Dimitriadis and Pistikopoulos [8] later developed an improved version for computing the *dynamic flexibility index* as follows.

$$\text{FI} = \max \delta \quad (32)$$

subject to

$$f_i(\mathbf{d}, \mathbf{z}(t), \mathbf{x}(t), \dot{\mathbf{x}}(t), \boldsymbol{\theta}(t)) = 0 \quad (33)$$

$$\max_{\boldsymbol{\theta}(t)} \min_{\mathbf{z}(t)} \max_{j,t} g_j(\mathbf{d}, \mathbf{z}(t), \mathbf{x}(t), \boldsymbol{\theta}(t), t) \leq 0 \quad (34)$$

$$\boldsymbol{\theta}^N(t) - \delta\Delta\boldsymbol{\theta}^-(t) \leq \boldsymbol{\theta}(t) \leq \boldsymbol{\theta}^N(t) + \delta\Delta\boldsymbol{\theta}^+(t) \quad (35)$$

where,  $f_i$  is the  $i$ th equality constraint in the design model (e.g., the dynamic mass or energy balance equation for a processing unit);  $g_j$  is the  $j$ th inequality constraint (e.g., a capacity limit);  $\mathbf{d}$  represents a vector which contains the design variables corresponding to the structure and equipment sizes of the plant;  $\mathbf{z}$  denotes a vector which contains the control variables that can be adjusted during operation, e.g., flows and utility loads;  $\mathbf{x}$  is a vector which contains the state variables that define the system, e.g., concentrations, temperatures and voltages;  $\boldsymbol{\theta}$  denotes the vector

**Table 1**  
Model parameters of battery [27].

Parameters	Symbol	Value, Unit
Nominal voltage	$E_0$	12 V
Rated capacity	$C_{O_2}$	6 Ah
Initial state-of-charge	$SOc_0$	100%
Internal resistance	$R_i$	0.02 $\Omega$
Exponential voltage	$A$	12.9646 V
Exponential capacity	$B$	0.294783 Ah
Polarization voltage Constants	$K_V$	0.0076 $\Omega$
Polarization resistance constants	$K_R$	0.0076 $\Omega$

which contains the uncertain parameters, e.g., the solar irradiation rate and power demand rate, etc. Finally, it is assumed that the operation horizon and the initial states are given, i.e.,  $t \in [0, H]$  and  $\mathbf{x}(0) = \mathbf{x}^0$ .

As mentioned before, to facilitate more realistic temporal flexibility analysis, it is necessary to consider both instantaneous and cumulative effects of uncertain disturbances. For this purpose, the aforementioned model must be further improved. Specifically, by keeping equations (32)–(35) intact, two types of uncertain parameters are introduced according to the following definitions.

$$\theta = \begin{bmatrix} \theta_1 \\ \theta_2 \end{bmatrix} \quad (36)$$

$$\dot{\theta}_2 = \theta_1 \quad (37)$$

This modified optimization problem, i.e., equations (32)–(37), can be handled with a straightforward solution strategy. In particular, all differential equations in (33) and (37) are first converted to a system of algebraic equations according to a credible numerical discretization technique and the resulting optimization problem is then solved with any existing algorithm for the steady-state flexibility analysis, e.g., see Biegler et al. [25]. Since the detailed computation procedure has already been provided in Adi and Chang [11,12,26], it is not repeated here for sake of brevity.

#### 4. Case studies

The case studies presented below are adopted mainly to demonstrate the important role of flexibility analysis in evaluating and synthesizing resilient designs for the hybrid power systems. The model parameters of battery, fuel cell and solar module are presented in Table 1 [27], Table 2 [28], and Table 3 [13], respectively. Since these components are interconnected with an electrical bus, the battery charging/discharging model can be expressed as:

**Table 2**  
Model parameters of FC module [28].

Parameters	Symbol	Value, Unit
Fuel cell temperature	$T$	52 $^\circ\text{C}$
Cross-section area of the electrolyte	$A_c$	126 $\text{cm}^2$
Distance between electrodes (electrode gap)	$d_e$	$6.0 \times 10^{-3}$ cm
Internal current density	$j_l$	$9.8 \times 10^{-3}$ A/cm $^2$
Symmetric factor at the anode	$\alpha_{\text{anode}}$	0.5, –
Symmetric factor at the cathode	$\alpha_{\text{cathode}}$	0.25, –
Anode standard exchange current density	$j_{0,\text{anode}}^{\text{ref}}$	$5 \times 10^{-4}$ A/cm $^2$
Cathode standard exchange current density	$j_{0,\text{cathode}}^{\text{ref}}$	$4 \times 10^{-7}$ A/cm $^2$
Anode flow constant	$k_{\text{anode}}$	$6.5 \times 10^{-2}$ mol/s atm
Cathode flow constant	$k_{\text{cathode}}$	$6.5 \times 10^{-2}$ mol/s atm
Anode volume	$V_{\text{anode}}$	$5 \times 10^{-3}$ m $^3$
Cathode volume	$V_{\text{cathode}}$	$1 \times 10^{-2}$ m $^3$
Back pressure	$p_{\text{BPR}}$	1 atm

**Table 3**  
Model parameters of PV module [13].

Parameters	Symbol	Value, Unit
Photocurrent at the standard testing condition (STC)	$I_{\text{phref}}$	8.21 A
Temperature coefficient	$\alpha$	0.0032 A/ $^\circ\text{C}$
Photocurrent losses due to charge carrier diffusion	$k_s$	890.01 A
Series resistance	$R_s$	0.71 $\Omega$
Diode ideality factor	$n_1$	1.08, –

$$\frac{dI}{dt} = I_{\text{batt}} = I_{\text{PV}} + I_{\text{FC}} - I_{\text{demand}} \quad (38)$$

Two time-dependent uncertain parameters are considered in all scenarios, i.e., the solar irradiation rate ( $S$ ) and the power demand ( $P_{\text{demand}}$ ). It is assumed that the solar irradiation rate may vary between  $\pm 40\%$  of the nominal level at any time. The *reference profile* of solar irradiation rate used in all case studies was taken from Fu and Rich [29] and the corresponding power output of a *standard PV module* can be found in Fig. 3. Since the module size can be adjusted so as to generate a proper design, the corresponding *nominal profile* was determined by multiplying the solar irradiation rate in Fig. 3 with a scale factor  $\gamma_{\text{PV}}$ . To confirm the feasibility of the proposed design approach, a series of preliminary cases were first studied with the arbitrarily-selected nominal demand profile given in Fig. 4. It was assumed that 30% positive and negative deviations from this nominal level can be anticipated at any instance. In the second set of test scenarios, the nominal demand profile and the corresponding expected deviations were extracted from realistic data to demonstrate the usefulness of flexibility analysis in practical applications. Finally, the hydrogen feed rate of fuel cell was treated as a control variable and it is allowed to vary between  $\pm 20\%$  of a baseline level. In this example, it is assumed that the reference feed rate of a standard cell is 14.4 kmol/h and the corresponding output current is 22.1 A. The baseline level of hydrogen feed rate in each case study was also determined by multiplying the above reference value with another scale factor  $\gamma_{\text{FC}}$ .

In order to ensure operability, Reeve [30] suggested to use a relatively large energy supply level, i.e.

$$\phi_{\text{SD}} = \frac{\text{Nominal daily energy supply level}}{\text{Nominal daily energy demand level}} = 1.2 \quad (39)$$

Note that the denominator can be computed by numerically integrating the power demand profile in Fig. 4. To facilitate quantitative discussions, let us also define.

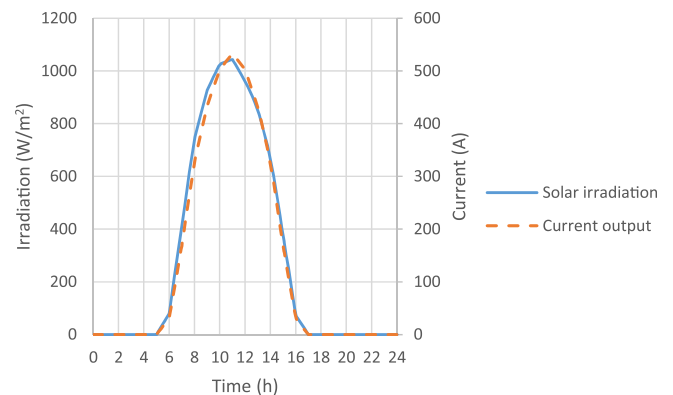


**Fig. 3.** Nominal profiles of solar irradiation rate and PV output current for both case study sets.

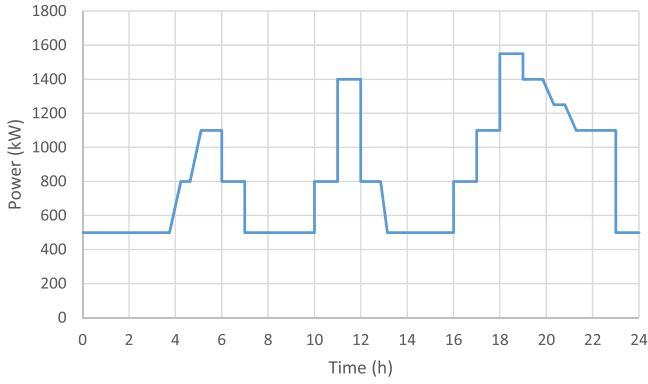


Fig. 4. Nominal profile of power demand in case study set 1.

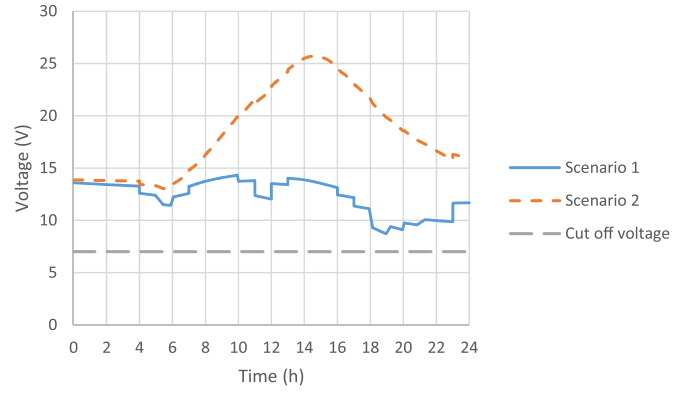


Fig. 6. Terminal voltage profile with  $r_{PV} = 0.4$ ,  $\phi_{SD} = 1.2$  and a battery size of 6 Ah in case study set 1.

$$r_{PV} = \gamma_{PV} \times \frac{\text{Time – averaged reference PV power}}{\text{Time – averaged nominal energy supply rate}} \quad (40)$$

$$r_{FC} = \gamma_{FC} \times \frac{\text{Time – averaged reference FC power}}{\text{Time – averaged nominal energy supply rate}} \quad (41)$$

$$r_{PV} + r_{FC} = 1 \quad (42)$$

Note that the denominators in equations (40) and (41) can be calculated according to the nominal daily energy supply level calculated according to a preset value of  $\phi_{SD}$  and equation (39). The time-averaged reference PV power in the numerator of equation (40) can be determined by integrating the output current in Fig. 3, multiplying the resulting definite integral by the reference terminal voltage, i.e., 12 V, and then dividing this product by 24 h. The reference FC power in the numerator of equation (39) is calculated by multiplying the output current of fuel cell ( $I_{FC}$ ) and the reference terminal voltage i.e., 12 V. Note that the former can be determined according to the empirical relation  $I_{FC} \approx k_{FC} F_{H_2}$  if the hydrogen feed rate is given, where  $k_{FC}$  is the fuel cell current constant, i.e., 1.531 Ah/kmol. By setting the ratio  $r_{PV}$ , the two scale factors ( $\gamma_{PV}$  and  $\gamma_{FC}$ ) can be computed on the basis of equations (40) and (41) and, then, the nominal profile of the solar irradiation rate and the baseline hydrogen feed rate can be established accordingly.

#### 4.1. Test results obtained with a fictitious demand profile

The values of flexibility index  $FI_t$  corresponding to the nominal demand profile in Fig. 4 and various different energy supply ratios were first computed by solving the aforementioned temporal flexibility index model for a constant battery size of 6 Ah and the results are summarized in Fig. 5. In the case when  $\phi_{SD}$  is 1.2, it can be observed that the system flexibility can in general be improved by raising  $r_{PV}$  until when it reaches approximately 0.93. Note that solar irradiation is strong in the daytime and the power produced with such a hybrid system should be more than enough for satisfying the immediate power demands during the day. The excess energy generated by the PV module can be stored in the battery and used later to cover the large demand in the evening. Thus, a low  $r_{PV}$  often fails to fulfill this requirement. In other words, the solar energy captured during the day may not be sufficient to cover the night-time demands if the PV module is too small. On the other hand, if  $\phi_{SD}$  is reduced from 1.20 to 1.05, a slightly lower  $FI_t$  can be anticipated at any value of  $r_{PV}$ . It can be observed from Fig. 5 that the profiles of  $FI_t$  in the range  $0.01 < r_{PV} < 0.92$  are quite similar in both cases. The flexibility index drops abruptly to zero when  $r_{PV}$  is just above 0.92 and  $\phi_{SD} = 1.05$ , while  $FI_t$  reaches 0 when  $r_{PV}$  is above 0.93 and  $\phi_{SD} = 1.20$ .

To verify the optimization results given in Fig. 5, the PVFC systems designed on the basis of the supply/demand ratio  $\phi_{SD} = 1.2$  were simulated at the extreme conditions in two scenarios, i.e., (1) when the solar irradiation is lowest and the power demand is highest, and (2) the solar irradiation is

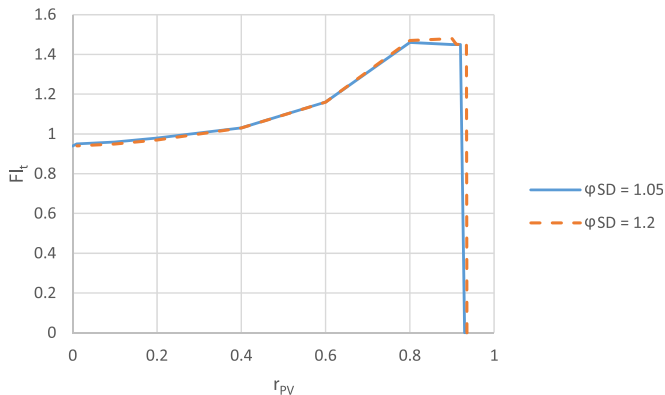


Fig. 5. Temporal flexibility index function  $FI_t(r_{PV})$  for a battery size of 6 Ah in case study set 1.

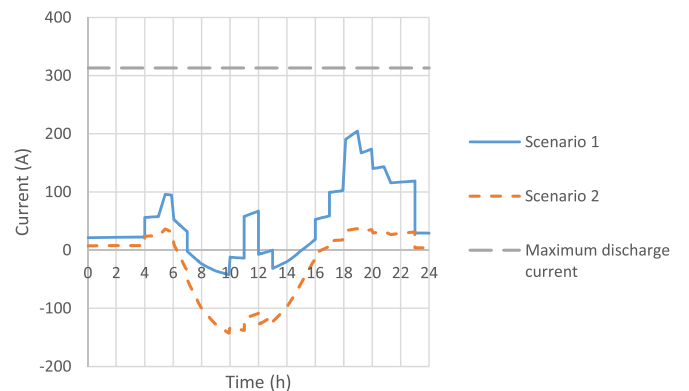


Fig. 7. Terminal current profile with  $r_{PV} = 0.4$ ,  $\phi_{SD} = 1.2$  and a battery size of 6 Ah in case study set 1.

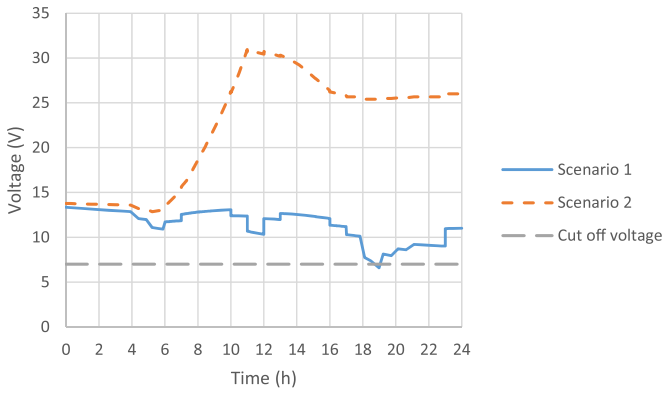


Fig. 8. Terminal voltage profile with  $r_{PV} = 0.2$ ,  $\phi_{SD} = 1.2$  and a battery size of 6 Ah in case study set 1.

highest and the power demand is lowest. It was found that the hydrogen flow rate must be maintained at its upper bound at all time in scenario 1 and, for scenario 2, the other way around. Figs. 6 and 7 show the simulation results obtained with a battery size of 6 Ah and  $r_{PV} = 0.4$ . From the fact that its flexibility index is 1.16, one can predict that the corresponding PVFC system should function normally over the entire time horizon. The positive current in Fig. 7 means that the battery is in the discharging mode, while a negative value means otherwise. Note also that the discharging current is still well below the maximum allowable value and, thus, the present selection of  $r_{PV} = 0.4$  should be considered as overdesign. Ideally the energy supply ratio should be set around 0.3 so as to achieve the flexibility target of  $FI_t = 1$ , which implies that the system can always work just well enough under the influence of the anticipated uncertain disturbances.

Let us next consider the system behavior in cases when  $r_{PV}$  is small and  $\phi_{SD} = 1.2$ . Fig. 8 shows the battery terminal voltage when  $r_{PV} = 0.2$ . Note that the minimum voltage level is reached after a very high current has been drawn from the battery shortly after 18 h and, consequently,  $FI_t = 0.97$  in this case. The same explanation can be adopted if the solar energy supply ratio is even smaller or as  $r_{PV} \rightarrow 0.0$ .

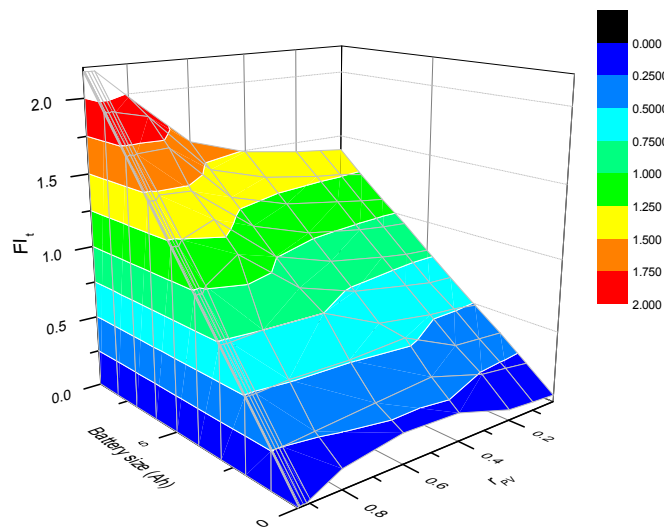


Fig. 9. The effects of energy supply ratio and battery size on the flexibility index in case study set 1 when  $\phi_{SD} = 1.2$ .

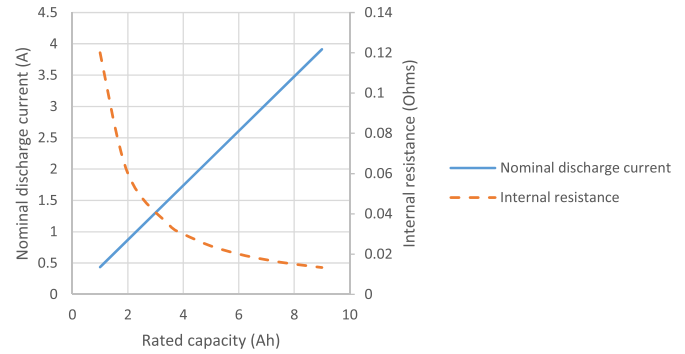


Fig. 10. Battery characteristics.

Finally, note that the flexibility index reaches a maximum when  $r_{PV} \approx 0.9$  and decreases quickly to zero if  $r_{PV} > 0.935$ . This is because, in the former case, the lowest total power provided by the FC unit and battery in initial time period, i.e., from 0 to 5 h, is just enough to satisfy the maximum possible demand. In this case, the minimum voltage level is reached after the demand current increase at a  $t \approx 5$  h. As the power supplied by fuel cell is reduced further to  $r_{PV} = 0.935$ , even the nominal demand can no longer be met and therefore the corresponding system is inoperable.

The aforementioned analysis has been repeated for other battery sizes and the corresponding results are depicted in Fig. 9 for  $\phi_{SD} = 1.2$ . It can be clearly observed that an increase in the battery size always results in a higher flexibility index at any given solar energy supply ratio. This is because the active constraint in the optimal solution is mainly associated with the minimum battery voltage, i.e., 7 V at  $t \approx 18$  h for  $r_{PV} = 0.2$ , when a large amount of current is drawn from the battery. By increasing the battery size, a larger flexibility index becomes attainable since the maximum discharge current of battery can be raised to a higher level. For the same cut off voltage i.e., 7 V, one can deduce from Ohm's law that a higher current is achievable if the internal resistance ( $R_i$ ) can be made lower. This internal resistance can in general be reduced by enlarging the battery capacity, while the corresponding nominal discharge current increased linearly. The above-mentioned trends have been verified in the present study (see Fig. 10) by using the

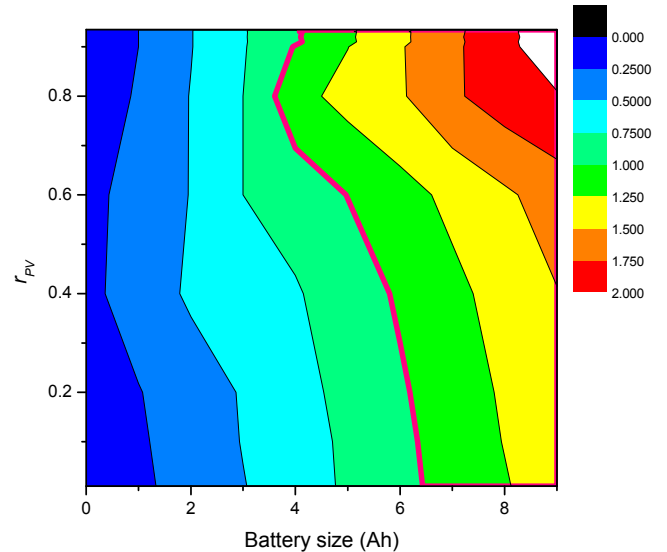


Fig. 11.  $FI_t$  contours in the feasible region of  $r_{PV}$  and battery size for case study set 1.

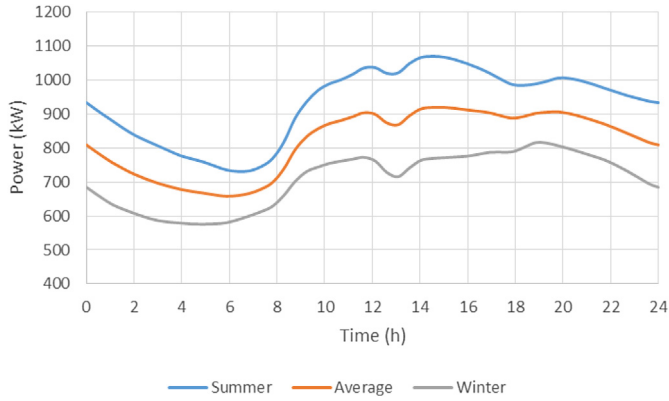


Fig. 12. The seasonal load curves of Taiwan Power Company in 2013 [32].

battery rating feature in Matlab® Simulink® [31] based on the model of Tremblay et al. [27]. To put it another way, with the same active constraint of cut off voltage, i.e., 7 V, the system flexibility should in general be improved with a larger battery size. It should also be noted that, for the smaller battery sizes below 6 Ah, the flexibility index of the system will drop quite linearly for all values of  $r_{PV}$ . A flexibility index of 1 is obviously desirable since any anticipated disturbance can be handled in the corresponding system. A larger  $Fl_t$  results in overdesign, while a smaller one implies inoperability. One can easily construct the contour of  $Fl_t = 1$  on a plane of  $r_{PV}$  versus battery size (see for example Fig. 11 for  $\phi_{SD} = 1.2$ ) to facilitate identification of a proper hybrid power design in any practical application.

4.2. Test results obtained with a realistic demand profile

As mentioned before, another nominal demand profile was adopted in the second set of case studies for the purpose of demonstrating the usefulness of the proposed approach in realistic applications. Fig. 12 shows the scaled-down load profiles of Taiwan Power Company on a typical day during winter and summer of 2013 [32]. The averaged value between the two is treated as the nominal level at any instance, while the maximum deviation was found to be  $\pm 18\%$  from this nominal level. It can also be observed from the data posted on the same website that the load variation is

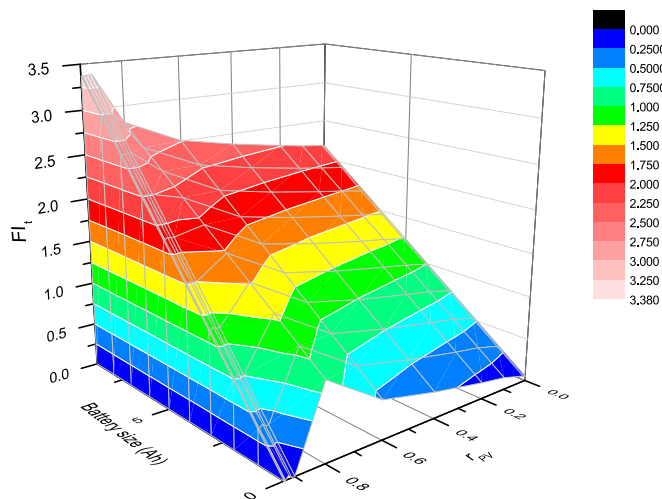


Fig. 13. Effects of energy supply ratio and battery size on the flexibility index in case study set 2 when  $\phi_{SD} = 1.2$ .

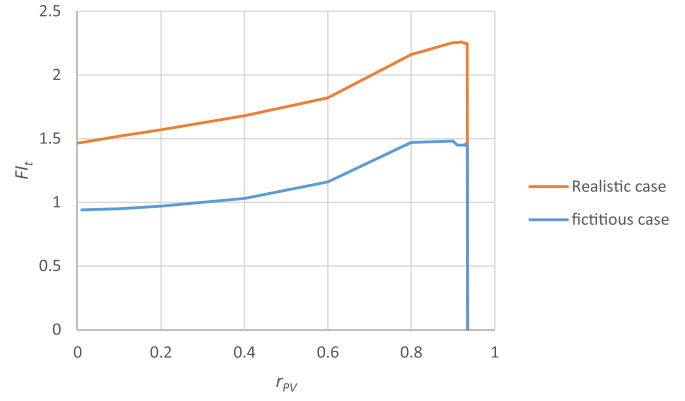


Fig. 14. Temporal flexibility index function  $Fl_t(r_{PV})$  for a battery size of 6 Ah in case study sets 1 and 2 when  $\phi_{SD} = 1.2$ .

periodic on a daily basis. A thorough flexibility analysis has been performed according to Figs. 3 and 12, and the results are summarized in Fig. 13.

The flexibility indices obtained with  $\phi_{SD} = 1.2$  and a battery size of 6 Ah are also plotted as a function of  $r_{PV}$  in Fig. 14 for both sets of case studies. It can be observed that, in general, the system flexibility increases with  $r_{PV}$  until reaching 0.934. This trend is primarily due to the fact that the daytime solar irradiation is strong and, thus, the power produced exceeds the immediate demand at any time during this period. The excess energy generated by the PV module can therefore be stored in the battery for later use. It is also worth noting that, for every combination of battery size and  $r_{PV}$ , the  $Fl_t$  obtained with the realistic demand profile is in general significantly higher than that with the fictitious one. By comparing Figs. 4 and 12, it can be seen that this improvement in flexibility clearly results from the less drastic demand variations required in the present case studies. In the preliminary cases presented in Section 4.1, the excess solar energy captured during the day may not be enough to cope with the sudden increase in night-time consumption if the PV module is too small, i.e.,  $Fl_t < 1$  at a low  $r_{PV}$ . This is obviously not a problem with the smoother demand curve considered in Fig. 12.

To verify the optimization results given in Fig. 13, the PVFC systems designed on the basis of the supply/demand ratio of 1.2 were again simulated by considering the extreme scenarios, i.e., (3) when the solar irradiation is at the lowest level and the power demand is the highest, and (4) the solar irradiation is at the highest level and the power demand is the lowest. It was found that the hydrogen flow rate must be maintained at its upper bound at all

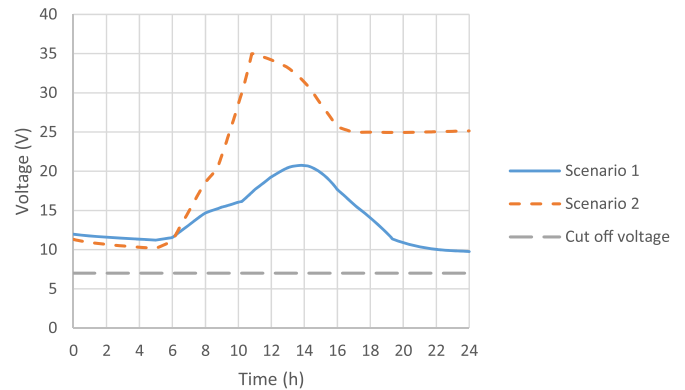


Fig. 15. Terminal voltage profile with  $r_{PV} = 0.6$ ,  $\phi_{SD} = 1.2$  and a battery size of 3 Ah in case study set 2.

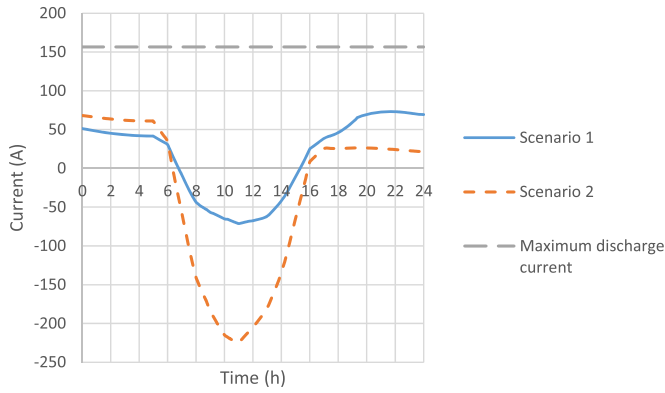


Fig. 16. Terminal current profile with  $r_{PV} = 0.6$ ,  $\phi_{SD} = 1.2$  and a battery size of 3 Ah in case study set 2.

time in scenario 3 and, for scenario 4, the other way around. Figs. 15 and 16 show the simulation results obtained with a battery size of 3 Ah and  $r_{PV} = 0.6$ . From the fact that its flexibility index is 1.13, one can predict that the corresponding PVFC system should function normally over the entire time horizon. The positive current in Fig. 15 means that the battery is in the discharging mode, while a negative value means otherwise. Note also that the discharging current is still well below the maximum allowable value and, thus, the present selection of  $r_{PV} = 0.6$  should be considered as over-design. Ideally the energy supply ratio should be set around 0.4 so as to achieve the flexibility target of  $FI_t = 1$ , which implies that the system can always work just well enough under the influence of the anticipated uncertain disturbances. Based on the load curve in Fig. 12, one can easily construct the contour of  $FI_t = 1$  on a plane of  $r_{PV}$  versus battery size (see for example Fig. 17 for  $\phi_{SD} = 1.2$ ) to facilitate identification of a proper hybrid power design in the corresponding application.

## 5. Conclusions

The proposed temporal flexibility analysis has been successfully applied to the PVFC hybrid power generation systems in this work. It can be clearly observed that (1) the operational flexibility is a

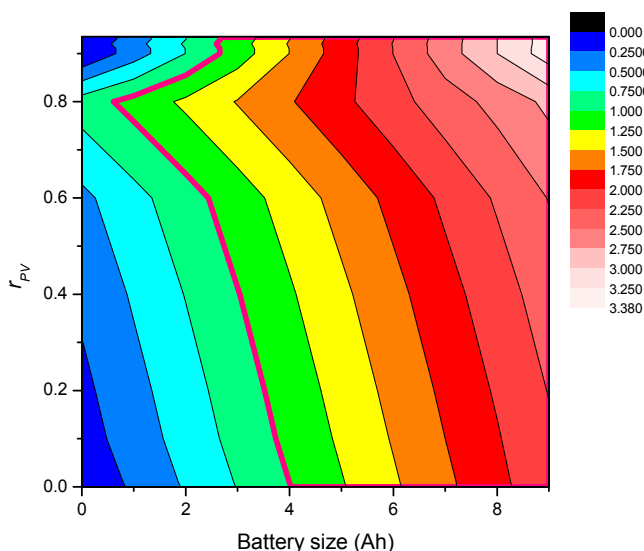


Fig. 17.  $FI_t$  contours in the feasible region of  $r_{PV}$  and battery size for case study set 2.

function of energy supply ratio and battery size and, (2) the cut-off voltage and the maximum discharge current of battery are the most critical constraints. Note also that the time profiles of energy supplies and demand also exert profound impacts on the system operability. From the simulation results obtained in two sets of case studies, one can see that the temporal flexibility analysis can indeed be used as an effective tool to address various design issues quantitatively. While in the future a rigorous cost analysis should obviously be performed, the capital and operating costs of each component can be assumed to be proportional to the equipment size and/or energy consumption level and, therefore, the trade-off between economic and operational incentives can still be assessed qualitatively on the basis of the proposed approach.

## Acknowledgment

The authors wish to thank Prof. W. Wu from the Department of Chemical Engineering, National Cheng Kung University, Taiwan for his useful insights for the hybrid power generation system.

## Nomenclature

### Acronyms

DAE	differential algebraic equation
FC	fuel cell
FI	flexibility index
PEM	polymer electrolyte membrane
PV	photovoltaic
PVFC	photovoltaic–fuel cell
SOC	state of charge
STC	standard testing condition

### Variables

$I_{PV}$	photovoltaic cell current
$I_{ph}$	light-generated current
$I_{d1}$	diffusion current from the base to emitter layers
$I_{d2}$	generation and re-combination current in the junction space charge region
$I_p$	current flowing through the shunt resistance ( $R_p$ )
$R_p$	shunt resistance
$R_s$	series resistance
$V$	terminal voltage
$I$	current
$I_{phref}$	photocurrent at the standard testing condition
$S$	solar irradiation rate
$S_{ref}$	solar irradiation rate reference value
$\alpha$	current temperature coefficient
$T_c$	cell temperature
$T_{cref}$	cell temperature reference level
$k_s$	photocurrent losses due to charge carrier diffusion
$n_1$	diode ideality factor
$E_g$	material bandgap energy
$V_t$	thermal voltage
$k$	Boltzmann's constant
$q$	charge of the electron
$k_r$	photocurrent losses due to charge carrier recombination
$n_2$	diode ideality factor
$U_{FC}$	fuel cells actual voltage
$U_{OCV}$	fuel cells open-circuit voltage
$\eta_{act}$	activation overpotential
$\eta_{conc}$	concentration overpotential
$\eta_{ohm}$	ohmic overpotential
$\Delta G_0$	change in Gibbs free energy at standard condition
$R$	gas constant

$p_{H_2}$	hydrogen partial pressure
$p_{O_2}$	oxygen partial pressure
$p_o$	operating pressure
$F$	Faraday's constant
$T_{FC}$	fuel cell temperature
$V_{anode}$	anode volume
$V_{cathode}$	cathode volume
$F_{H_2}$	hydrogen molar flow rate
$F_{O_2}$	oxygen molar flow rate
$k_{anode}$	anode flow constant
$k_{cathode}$	cathode flow constant
$p_{BPR}$	cell back pressure
$\beta$	transfer coefficient
$j$	electrical current density
$j_o$	exchange current density on the catalytic surfaces
$C_{O_2}$	oxygen concentration
$C_{H_2O}$	water vapor concentration
$j_o^{ref}$	standard exchange current density
$\Delta G$	change in Gibbs free energy
$\eta_{conc,anode}$	anode concentration overpotential
$\eta_{conc,cathode}$	cathode concentration overpotential
$j_{anode}$	anode current density
$j_{cathode}$	cathode current density
$j_L$	internal current density
$\eta_{ohm,e}$	electrical conductors overpotential
$I_{FC}$	cell current density
$R_{ec}$	equivalent electrical resistance
$\eta_{ohm,m}$	electrolyte membrane Ohmic overpotential
$R_{ic}$	electrolyte membrane ionic resistance
$d_e$	electrode gap width
$A_c$	electrolyte body cross-section area
$\sigma_m$	electrolyte membrane ionic conductivity
$\lambda$	electrolyte membrane water content
$\phi$	water vapor activity
$k_{FC}$	FC module current empirical constant
$V_{batt}$	battery voltage
$E_0$	reference constant
$V_{pol}$	polarization voltage
$R_{pol}$	polarization resistance
$K_V$	polarization voltage constant
$K_R$	polarization resistance constant
$Q$	battery capacity
$A$	exponential zone amplitude
$B$	inverse of zone time constant
$R_i$	internal resistance
$I_{batt}$	battery current
$I_{batt}^*$	filtered current
$it$	actual battery charge
SOC	state of charge
$i_{batt}^{max}$	maximum discharge current
$i$	set of equality constraints
$j$	set of inequality constraints
$f_i$	$i$ th equality constraint
$g_j$	$j$ th inequality constraint
$d$	design variables vector
$z$	control variables vector
$x$	state variables vector
$\theta$	uncertain parameters vector
$\theta^N$	nominal parameter value
$\Delta\theta^+$	positive expected deviations
$\Delta\theta^-$	negative expected deviations
$d$	vector of design variables
$\theta$	vector of uncertain parameters
$t$	time
$H$	operation horizon

$FI_t$	temporal flexibility index
$\delta$	deviation due to uncertainties
$P_{demand}$	power demand
$\gamma_{PV}$	photovoltaic cell scale factor
$\gamma_{FC}$	fuel cell scale factor
$r_{PV}$	photovoltaic cell power ratio
$r_{FC}$	fuel cell power ratio
$\phi_{SD}$	daily energy supply ratio

## References

- [1] Sadri JA, Hooshmand P. A survey study on hybrid photovoltaic system: technical and economical approach. *J Basic Appl Sci Res* 2012;2:209–14.
- [2] Hwang JJ, Chang WR, Su A. Development of a small vehicular PEM fuel cell system. *Int J Hydrogen Energy* 2008;33:3801–7.
- [3] El-Aal AEMMMAA. Modeling and simulation of a photovoltaic fuel cell hybrid system [dissertation]. Germany: University of Kassel; 2005.
- [4] Li CH, Zhu XJ, Cao GY, Sui S, Hu MR. Dynamic modeling and sizing optimization of stand-alone photovoltaic power systems using hybrid energy storage technology. *Renew Energy* 2009;34:815–26.
- [5] Tesfahunegn SG. Fuel cell assisted photovoltaic power systems [dissertation]. Norway: Norwegian University of Science and Technology; 2012.
- [6] Banos R, Manzano-Agugliaro F, Montoya FG, Gil C, Alcayde A, Gómez J. Optimization methods applied to renewable and sustainable energy: a review. *Renew Sustain Energy Rev* 2011;15:1753–66.
- [7] Bajpai P, Dash V. Hybrid renewable energy systems for power generation in stand-alone applications: a review. *Renew Sustain Energy Rev* 2012;16:2926–39.
- [8] Dimitriadis VD, Pistikopoulos EN. Flexibility analysis of dynamic systems. *Ind Eng Chem Res* 1995;34:4451–62.
- [9] Swaney RE, Grossmann IE. An index for operational flexibility in chemical process design. Part I: formulation and theory. *AIChE J* 1985;31:621–30.
- [10] Swaney RE, Grossmann IE. An index for operational flexibility in chemical process design. Part II: computational algorithms. *AIChE J* 1985;31:631–41.
- [11] Adi VSK, Chang CT. SMDDS design based on temporal flexibility analysis. *Desalination* 2013;320:96–104.
- [12] Adi VSK, Chang CT. A mathematical programming formulation for temporal flexibility analysis. *Comput Chem Eng* 2013;57:151–8.
- [13] Shen WX, Choo FH, Wang P, Loh PC, Khoo SY. Development of a mathematical model for solar module in photovoltaic systems. In: 2011 6<sup>th</sup> IEEE Conference on Industrial Electronics and Applications (ICIEA); 2011 June 21–23; Beijing, China. New Jersey: IEEE; 2011. p. 2056–61.
- [14] Duffie JA, Beckman WA. Solar engineering of thermal process. 4th ed. New York: Wiley; 1991. p. 745–73.
- [15] Rosell JI, Ibanez M. Modeling power output in photovoltaic modules for outdoor operating conditions. *Energy Convers Manage* 2006;47:2424–30.
- [16] Barbir F. PEM fuel cells: theory and practice. Burlington: Elsevier/Academic Press; 2005.
- [17] Wu W, Zhou YY, Lin MH, Hwang JJ. Modeling, design and analysis of a stand-alone hybrid power generation system using solar/urine. *Energy Convers Manage* 2013;74:344–52.
- [18] Kordesch K, Simader GR. Fuel cells and their applications. Weinheim: VCH; 1996.
- [19] Bernardi DM, Verbrugge MW. A mathematical model of the solid-polymer-electrolyte fuel cell. *J Electrochem Soc* 1992;139:2477–91.
- [20] Amphlett JC, Baumert RM, Mann RF, Peppley BA, Roberge PR. Performance modeling of the Ballard Mark IV solid polymer electrolyte fuel cell: II. Empirical model development. *J Electrochem Soc* 1995;142:9–15.
- [21] Chang WR, Hwang JJ. Effect of clamping pressure on the performance of PEM fuel cells. *J Power Sources* 2007;166:149–54.
- [22] Wang JT, Savinell RF. Simulation studies on the fuel electrode of a H<sub>2</sub>-O<sub>2</sub> polymer electrolyte fuel cell. *Electrochim Acta* 1992;37:2737–45.
- [23] Hwang JJ. Thermal-electrochemical modeling of a proton exchange membrane fuel cell. *J Electrochem Soc* 2006;153:A216–24.
- [24] Tremblay O, Dessaint LA. Experimental validation of a battery dynamic model for EV applications. *World Electric Veh J* 2009;3:1–10.
- [25] Biegler LT, Grossmann IE, Westerberg AW. Systematic methods of chemical process design. New Jersey: Prentice-Hall; 1997. p. 690–714.
- [26] Adi VSK, Chang CT. Dynamic flexibility analysis with differential quadratures. *Comput Aid Chem Eng* 2012;31:260–4.
- [27] Tremblay O, Dessaint LA, Dekkiche AL. A generic battery model for the dynamic simulation of hybrid electric vehicles. In: 2007 IEEE Vehicle Power and Propulsion Conference (VPPC); 2007 Sept 9–12; Texas, USA. New Jersey: IEEE; 2007. p. 284–9.
- [28] Hwang JJ, Lai LK, Wu W, Chang WR. Dynamic modeling of a photovoltaic hydrogen fuel cell hybrid system. *Int J Hydrogen Energy* 2009;34:9531–42.
- [29] Fu P, Rich PM. Design and implementation of the solar analyst: an ArcView extension for modeling solar radiation at landscape scales [Internet]. In: Proceedings of the 19<sup>th</sup> Annual ESRI User Conference, San Diego, USA; 1999 [cited 2014 July 20]. Available from: <http://www.esri.com/library/userconf/proc99/proceed/papers/pap867/p867.htm>.

- [30] Reeve WD. DC power system design for telecommunications. IEEE press telecommunications handbook series. New Jersey: IEEE Press; 2007.
- [31] The MathWorks, Inc. Battery: implement generic battery model. [Internet]. Massachusetts: The MathWorks, Inc.; © 1994–2014. [cited 2014 April 10]. Available from: [www.mathworks.com/help/physmod/sps/powersys/ref/battery.html](http://www.mathworks.com/help/physmod/sps/powersys/ref/battery.html).
- [32] Cheng G. 電力系統負載曲線 (Load curve). [Internet]. WordPress.com. [cited 2014 July 20]. Available from: <http://gordoncheng.wordpress.com/2010/09/06/%E9%9B%BB%E5%8A%9B%E7%B3%BB%E7%B5%B1%E8%B2%A0%E8%BC%89%E6%9B%B2%E7%B7%9Aload-curve/>.